ISSN:2584-2706 DOI: https://doi.org/10.67317/IJMSRT26AUG057

Optimising Chilled Cast Iron Grinding Wheels for Food Processing through Microstructure Control

Sikiru Kayode Sanusi
Department of Metallurgical Engineering,
The Federal Polytechnic, Offa,
Kwara State, Nigeria

Hassan Onimisi Yakubu
Department of Metallurgical Engineering,
The Federal Polytechnic, Offa
Kwara State

Abstract
Domestic food processing across West Africa depends on cast iron grinding wheels with a white iron surface layer containing a continuous cementite network for wear resistance and a grey iron core for structural support, yet these components suffer severe wear degradation. The wear coefficient evolution as a function of heat treatment temperature has not been quantified, nor has the friction-wear coupling mechanism been established, leaving manufacturers without guidance. Specimens from a locally manufactured wheel (3.35 wt% C, 1.80 wt% Si) were subjected to annealing, normalising, quenching, and tempering at 700°C, 750°C, and 800°C. Hardness was measured by Brinell testing, microstructures by optical microscopy, and wear performance by the Archard model with microstructure-dependent coefficients. The as-cast material exhibited 229 HBW, while all heat treatments reduced hardness; water quenching did not produce martensite due to 1.80 wt% Si limiting hardenability. Calculated mass loss increased from 250 mg to 310–3,400 mg for heat-treated conditions, representing up to 1,300% increase, as thermal energy promotes cementite decomposition. Heat treatment increases the wear coefficient by up to 830% and transitions wear from micro-cutting to ploughing. The as-cast condition provides 21-month estimated service life compare to 2-month for annealed wheels, representing a 14-fold annual cost reduction. Manufacturers should prioritise casting conditions over thermal processing. This study introduces the first microstructure-specific wear coefficient framework and economic life-cycle cost model for these wheels.

Keywords:
Abrasive wear resistance; Archard wear model; cementite decomposition; chilled cast iron; food processing equipment

1. Introduction

Across West Africa, domestic food processing relies extensively on cast iron grinding wheels that experience severe wear degradation during daily operation, imposing recurrent economic burdens on small-scale processors. These components are manufactured as chilled cast irons, developing a white iron surface layer containing a continuous cementite network that delivers abrasion resistance, while a grey iron core provides structural support. The service performance of these wheels is primarily determined by microstructural characteristics influenced by alloy composition, solidification conditions, and any subsequent thermal processing. Cooling rates during solidification significantly determine microstructure, with rates exceeding 100°C/min favouring white iron formation while rates

ISSN:2584-2706 DOI: https://doi.org/10.67317/IJMSRT26AUG057

below 30°C/min allow grey iron structures to develop (Adeyemo *et al.,* 2023; Taiwo *et al.,* 2024). Various heat treatment processes—annealing, normalising, quenching, and tempering—are commonly employed to alter cast iron properties (Kibble and Pearce, 2023; Ochulor *et al.,* 2023), yet their effects on chilled cast iron, which derives its performance from a metastable white iron surface layer, remain poorly understood and cannot be inferred from studies on other cast iron types.

The tribological performance of these grinding wheels is governed primarily by the hardness ratio between silica abrasive particles (~1100 HV) and the specimen surface, with $H_{abrasive}/H_{specimen}$ = 5.5-9.3 confirming rigid abrasive behaviour. In chilled cast iron, the continuous cementite network (Fe_3C, ~1500 HV) embedded in a pearlitic matrix resists abrasive penetration, while the cementite fraction and morphology determine material removal. Manufacturers of these wheels, typically small to medium foundries using static casting methods, face a practical decision whether to apply post-casting heat treatment or use wheels in the as-cast condition, but lack evidence-based guidance due to the absence of systematic studies for this specific application. From a thermodynamic perspective, cementite is metastable in the iron-carbon system, and heating provides thermal activation energy for carbon diffusion and graphitisation (Callister and Rethwisch, 2020). The alloy contains 1.80 wt% silicon, a graphitising element that weakens Fe-C bonds and lowers decomposition activation energy (Sudiyanto *et al*., 2023; Darmawan *et al.,* 2025), with cooling rate after austenitisation determining whether carbon reprecipitated as cementite or graphite.

Despite widespread use of chilled cast iron grinding wheels across West Africa, comprehensive evaluation of heat treatment effects on their microstructure and tribological performance has not been undertaken. The wear coefficient values characteristic of the chilled condition and each heat-treated microstructure remain to be experimentally determined, the friction-wear coupling mechanism through which cementite decomposition simultaneously influences wear volume, wear coefficient, and ploughing friction has received little attention, and the economic consequences for small-scale processors remain speculative. The central hypothesis of this investigation is that post-casting heat treatment degrades tribological performance through thermally-activated decomposition of the metastable cementite network, manifesting through three mechanisms: decreased hardness following Arrhenius-type kinetics with an activation energy of 200-250 kJ/mol for carbon diffusion, increased estimated wear coefficients from 1.2×10^{-4} toward values exceeding 8.0×10^{-4}, and a mechanistic transition from cementite-dominated micro-cutting to ferrite-dominated ploughing. The null hypothesis posits no significant effect or that hardness reduction is offset by microstructural toughening. This hypothesis is grounded in thermodynamic principles: cementite is metastable relative to graphite and ferrite, with free energy difference of approximately -2.5 kJ/mol at 727°C, and 1.80 wt% silicon lowers decomposition activation energy, making graphitisation kinetically accessible during the 1-hour soak. However, this hypothesis remains untested for this specific composition and application, as prior studies have focused on fully white irons (400-600 HBW) or malleablising treatments (>900°C), neither representing the present chilled cast iron with its duplex structure. The critical scientific question is whether thermal energy at subcritical (700°C) and above-eutectoid (750-800°C) temperatures initiates' detectable graphitisation translating into wear coefficient increases that cannot be predicted from hardness alone.

This investigation presents theoretical wear estimates only. The study did not conduct experimental abrasion testing. The wear coefficient values and mass loss calculations are predictions based on the Archard model, not experimental measurements. While the strong correlation with hardness supports the comparative ranking, quantitative values require experimental validation.

This investigation addresses three research questions: the quantitative relationship between heat treatment temperature and resulting Brinell hardness for each treatment type; how microstructure-dependent wear coefficients vary across conditions and whether hardness alone adequately predicts wear resistance; and the mechanistic pathway linking cementite decomposition to wear mechanism changes and the economic implications for food processors. The study introduces an integrated approach establishing quantitative relationships between heat treatment temperature, cementite decomposition kinetics, microstructure-dependent wear coefficients, and life-cycle economics. It demonstrates for the first time that water quenching fails to induce martensite formation in this composition owing to 1.80 wt% silicon, and provides the first quantitative evidence that even subcritical treatment at 700°C measurably compromises wear resistance through incipient graphitisation. These findings aim to support processing optimisation for improved performance and

ISSN:2584-2706 DOI: https://doi.org/10.67317/IJMSRT26AUG057

extended service life, providing actionable recommendations for manufacturers and end-users across West Africa.

2. Materials And Methods

2.1 Materials

A grinding wheel was obtained from a local manufacturer in Nigeria, with chemical composition provided by the supplier and recorded in Table 1. The wheel measured approximately 230 mm in outer diameter, 8 mm rim thickness, and 22 mm arbour hole diameter, consistent with commercial grinding plates used for domestic food processing in West Africa (MEDID, 2025). Figure 1 shows the wheel in as-cast and, used and broken conditions, illustrating typical wear and failure modes.
Material evaluation referenced EN 12513:2011 for abrasion-resistant cast irons, ASTM A532/A532M-21 for abrasion-resistant cast irons, EN 1561:2011 for grey cast irons, EN 1562:2019 for malleable cast irons, EN 1563:2018 for spheroidal graphite cast irons, and ASTM G65-16 for dry sand/rubber wheel abrasion testing (European Committee for Standardization, 2011; ASTM International, 2021; ASTM International, 2016). These standards specify 400–600 HBW for fully white iron grades, confirming the material classification as chilled cast iron.
This study did not involve direct testing on human subjects, animals, or food products. The research focused on material characterisation and wear performance evaluation of grinding wheels. However, given the application in food processing, the findings have implications for food safety, which are discussed in Section 4.5. All laboratory procedures were conducted in accordance with standard materials testing protocols.

Table 1. Chemical composition of the as-received cast iron grinding wheel.

Elements	Iron (Fe)	Carbon (C)	Silicon (Si)	Manganese (Mn)	Sulphur (S)	Phosphorus (P)
Composition (wt%)	Balance	3.35	1.80	0.65	0.10	0.10

Iron content is reported as the balance and includes trace elements typically present in commercial cast irons (Ti, V, Cr, Ni, Mo, Cu, and so on) which were not analysed in this study.

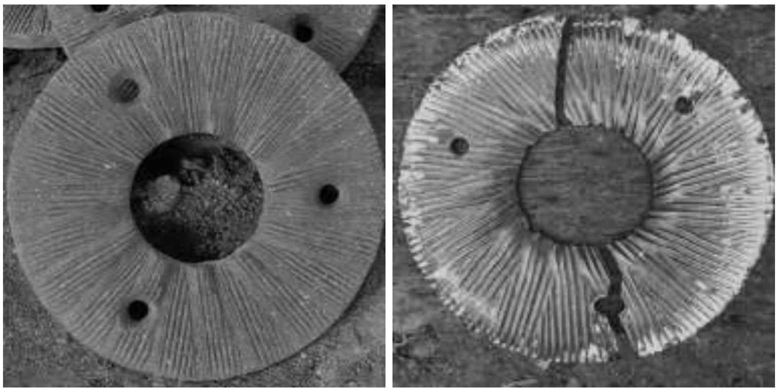

As-Cast Used and Broken

Figure 1: Grinding wheels in as-cast condition (left) and used and broken condition (right). The wheel measures approximately 230 mm outer diameter, 8 mm rim thickness, and 22 mm arbour hole diameter. No scale bar is included as the images show the full wheel dimensions.

2.2 Carbon Equivalent

Carbon equivalent was calculated using the formula:

$$CE = C\% + \frac{(Si\% + P\%)}{3} \quad (1)$$

CE = 3.35 + (1.80 + 0.10)/3 = 3.35 + 1.90/3 = 3.35 + 0.633 = 3.983 ≈ 3.99%

The calculated carbon equivalent indicates a hypoeutectic cast iron composition that favours carbide formation under rapid cooling conditions and is characteristic of chilled cast iron applications. The carbon content of 3.35% is relatively high for fully white iron, which typically requires 2.5–3.0% carbon to retain carbon as iron carbide (Callister and Rethwisch, 2020).

Figure 2 presents the iron-carbon metastable phase diagram (Okamoto, 2008; Callister and Rethwisch, 2020). The alloy composition at 3.35% C and CE of 3.99% is shown by the dashed red line. Rapid cooling promotes the metastable eutectic reaction (L → γ + Fe_3C) at 1147°C to form white iron, while slow cooling permits the stable eutectic reaction (L → γ + graphite) at 1153°C to form grey iron. The eutectoid reaction at 727°C influences the final room-temperature microstructure.

The critical cooling rate for white iron formation depends on composition, particularly carbon equivalent and silicon content (Yescas-Gonzalez and Bhadeshia, 2001). For the composition studied (CE = 3.99wt%, 1.80wt% Si), the specific values of 100°C/min for surface chill and 30°C/min for core graphitisation correspond to the rim section thickness of approximately 6 mm (Adeyemo et al., 2023; Kostyleva *et al*., 2019). The closeness of stable and metastable equilibrium lines explains why cooling rate determines whether carbon precipitates as graphite or cementite (Kibble and Pearce, 2023)

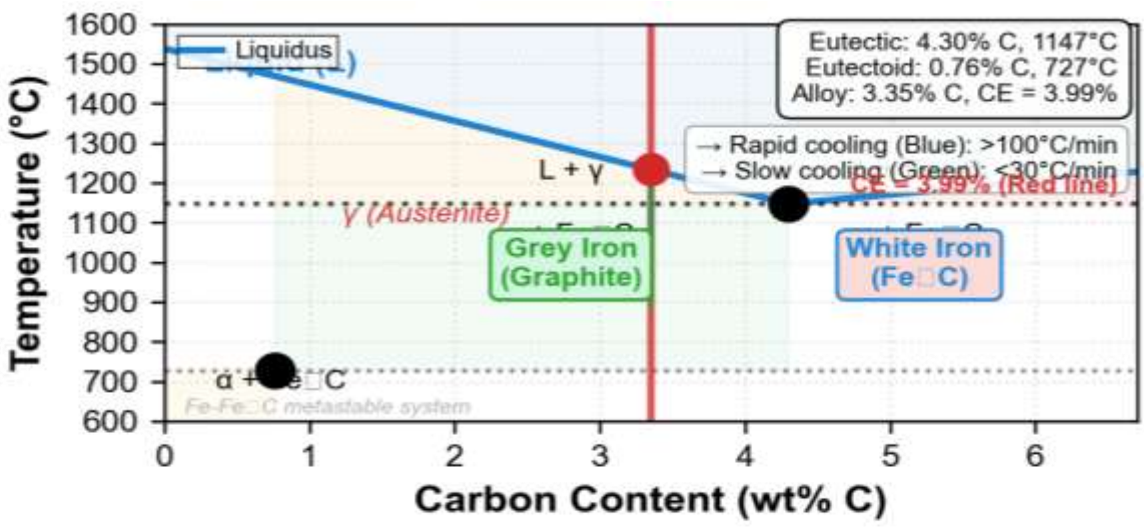

Figure 2. Iron-carbon (Fe-Fe_3C) metastable phase diagram showing the eutectic region. The alloy composition at 3.35 wt% C (CE = 3.99 wt%) is indicated by the red line. Metastable eutectic at 1147°C; stable eutectic at 1153°C; eutectoid at 727°C. The phase diagram was constructed based on data from Okamoto (2008) and Callister and Rethwisch (2020)

2.3 Sample Preparation and Heat Treatment

The grinding wheel of dimension: 230 mm outer diameter, 8 mm rim thickness, 22 mm arbour hole diameter (MEDID, 2025) was sectioned into fifteen rectangular specimens measuring 20.0 ± 0.5 mm × 15.0 ± 0.5 mm × 8.0 ± 0.3 mm using a precision cut-off machine (ATM Brillant 220, ATM GmbH, Germany) equipped with a cubic boron nitride (CBN) cutting wheel operating at 2800 rpm under continuous water cooling at a feed rate of 1.0 mm/s. The 8.0 mm thickness corresponds to the wheel rim section. All fifteen specimens were cut from the same wheel to ensure compositional and microstructural homogeneity across the experimental conditions.

ISSN:2584-2706 DOI: https://doi.org/10.67317/IJMSRT26AUG057

Specimens were randomly divided into five groups of three specimens each: as-cast (n=3), annealed (n=3), normalised (n=3), quenched (n=3), and tempered (n=3). This sample size of n=3 per condition was selected to meet the minimum repeatability requirements specified in ASTM E10-18 (Section 13.1) for hardness testing and to enable statistical validation through one-way analysis of variance (ANOVA) with $\alpha = 0.05$.

Heat treatment was performed in a muffle furnace (Nabertherm N60/H, Nabertherm GmbH, Germany; 20 L chamber) equipped with a Eurotherm 3216 PID temperature controller and two type K thermocouples (1.5 mm diameter). Furnace temperature uniformity was verified at ±4°C across the working zone through a five-point temperature survey before each treatment. All thermocouples were calibrated against a NIST-traceable reference thermocouple (±0.5°C accuracy) using a Fluke 9170 Metrology Well at 700°C, 750°C, and 800°C.

Three austenitising temperatures were selected: 700°C (subcritical, below the 727°C eutectoid), 750°C (incipient austenitisation), and 800°C (full austenitisation). For each temperature, three independent specimens were processed simultaneously in each heat treatment group to ensure identical thermal histories. The three specimens within each group were placed on the same alumina plate, positioned symmetrically within the furnace working zone to maintain uniform heating conditions. The heating rate was controlled at 10.0 ± 0.5°C/min using 50°C per 5 min ramp segments, monitored by a Graphtec GL840 data logger at 1 Hz sampling rate. Upon reaching the target temperature, specimens were held for 60 ± 1 minutes. The holding time was calculated using the equation $t = K \times a^2$, where t is the holding time in minutes, K is the thermal diffusivity constant (31.25 min/mm² for cast iron), and a is the half-thickness of the specimen in mm (4.0 mm). This yielded a minimum required hold of 50 minutes; therefore, 60 minutes was selected to ensure complete thermal equilibration. Temperature stability during holding was maintained within ±2°C.

Four cooling regimes were applied after the 60-minute hold at each austenitising temperature (700°C, 750°C, and 800°C):

Annealing: Furnace power was switched-off and the furnace door was sealed. Cooling rate was measured at 1 Hz using the data logger: 0.9 ± 0.1°C/min from the austenitising temperature to 500°C; 0.4 ± 0.1°C/min from 500°C to 200°C. Total cooling time from the austenitising temperature to 25°C was 14.2 ± 0.3 hours. Each of the three specimens in the annealing group was subjected to identical cooling conditions within the furnace.

Normalising: Specimens were removed from the furnace and placed on a wire mesh in still air at 25 ± 2°C and 45 ± 5% relative humidity. All three specimens in the normalising group were removed simultaneously and placed adjacent to each other on the same wire mesh to ensure identical air flow and cooling rates. A surface-mounted thermocouple attached to a dummy specimen of identical dimensions measured the cooling rate: 9.6 ± 0.8°C/min from the austenitising temperature to 500°C; 3.2 ± 0.4°C/min from 500°C to 200°C. Total cooling to 100°C was 45.3 ± 2.1 minutes, producing partial graphitisation.

Water Quenching: Specimens were rapidly transferred from the furnace to a 50 L tank of demineralised water (25 ± 2°C, electrical resistivity ≥18 MΩ·cm) with an agitator providing a flow velocity of 2.5 m/s. The three specimens in the quenching group were transferred simultaneously using a custom-designed basket to ensure identical transfer times and quenching conditions. Transfer time from furnace opening to full immersion was 3.2 ± 0.5 seconds. Cooling was monitored using a 0.5 mm diameter thermocouple embedded in a dummy specimen of identical dimensions: 82.5 ± 4.8°C/s from the austenitising temperature to 500°C (vapour phase cooling), peak cooling rate of 96.3 ± 3.7°C/s at 650°C (nucleate boiling), decreasing to 12.6 ± 1.2°C/s from 300°C to 100°C (convection cooling). Specimens were held in the water bath for 5 minutes to ensure complete cooling to bath temperature.

Tempering: Water-quenched specimens were reheated to 400 ± 2°C at a rate of 15.0 ± 0.5°C/min, held for 60 ± 1 minutes, and cooled in still air to relieve residual stresses from quenching. All three tempered specimens were processed together to ensure identical reheating and cooling conditions.

All cooling rate measurements were performed using a National Instruments NI 9213 data acquisition system (24-bit resolution) at 1000 Hz sampling rate for quenching and 1 Hz for slower cooling processes. Thermocouple response time was less than 0.1 second. Cooling curves were analysed using NI DIAdem 2021 software. Figure 3 presents the measured thermal history profiles for all treatments

ISSN:2584-2706 **DOI: https://doi.org/10.67317/IJMSRT26AUG057**

at 800°C; identical cooling profiles were applied at 700°C and 750°C with correspondingly lower peak temperatures.

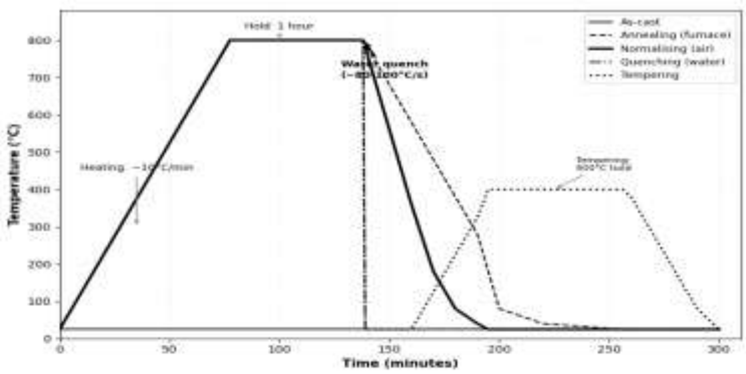

Figure 3. Thermal history profiles for heat treatments at 800°C, with the same profiles applied at 700°C and 750°C at reduced peak temperatures. All treatments involved heating at ~10°C/min with 1-hour hold. Cooling: annealing at ~1°C/min, normalising at ~10°C/min, quenching at ~80–100°C/s, and tempering by water quenching from austenitising temperature followed by reheating to 400°C for 1 hour and air cooling. As-cast condition shown as baseline.

2.4 Hardness Testing

Hardness testing was performed using a ZwickRoell ZHU250 universal hardness tester (ZwickRoell GmbH, Germany) with a 10.000 ± 0.005 mm tungsten carbide ball indenter conforming to ISO 6506-1:2014. A 750 kgf (7.355 kN) load was applied at 5 mm/s, held for 15.0 ± 0.5 seconds, and unloaded. The machine was calibrated using certified Brinell hardness reference blocks (HRC 15 N, 25 N, and 35 N) traceable to NIST.

For each condition, all three independent specimens (n=3 per condition) were tested, with three indentations per specimen (nine measurements total per condition). Indentations were spaced at least 25 mm apart (greater than three times indentation diameter) and at least 5 mm from edges, following ASTM E10-18. Indentation diameters were measured using an integrated optical system (resolution 0.01 mm, 40× magnification), with two perpendicular diameters averaged per indentation. Brinell hardness was calculated using Equation (2) and verified against ASTM E10-18 conversion tables. The mean and standard deviation for each condition were calculated from the nine individual measurements (three specimens' × three indentations per specimen), with standard deviations representing the measurement scatter across both specimens and indentations.

$$HB = \frac{2P}{\pi D\left(D-\sqrt{D^2-d^2}\right)} \quad (2)$$

Where:

- P = applied load (kgf)
- D = diameter of ball indenter (mm)
- d = diameter of indentation (mm)

2.5 Microstructural Examination

Metallographic specimens were sectioned parallel to the 8 mm thickness direction and mounted in epoxy resin (Struers EpoFix, 25 mm diameter). Grinding was performed on a Struers LaboPol-30 automatic machine (Struers A/S, Denmark) with a 300 mm aluminium oxide disc at 150 rpm using sequential SiC papers: P120 (30 N, 3 min), P320 (25 N, 4 min), P400 (20 N, 3 min), and P600 (15 N, 3 min), with water cooling at 1 L/min. Ultrasonic cleaning in ethanol for 2 minutes was applied between steps.

ISSN:2584-2706 DOI: https://doi.org/10.67317/IJMSRT26AUG057

Polishing used a MD-Mol cloth disc at 150 rpm: coarse polishing with 3 µm diamond suspension (Struers DiaPro, 20 N, 5 min) and final polishing with 1 µm alumina suspension (0.05 µm, 15 N, 7 min). Ultrasonic cleaning (Elmasonic P30H, 37 kHz) for 3 minutes followed each stage.
Etching was performed by immersion in 2% Nital (2.0 ± 0.1 cm^3 HNO_3 in 98.0 ± 0.1 cm^3 methanol) for 5.0 ± 0.1 seconds, rinsed in distilled water (10 s), ethanol (10 s), and dried in warm air at 40°C for 30 seconds. Fresh etchant was prepared for each batch.
Microstructural examination was performed using an Olympus BX51M metallurgical microscope with 10× objective (NA 0.30) providing ×100 total magnification. Images were captured with an Olympus DP73 digital camera (17.28 MP, 6.45 µm/pixel) using Olympus cellSens Standard v1.18. Standardised acquisition parameters: white balance 3200 K, exposure 1.25 ms, gain 1.0×, 24-bit TIFF format. Six fields of view per specimen were captured (centre, edge, and quarter positions). Scale bars (100 µm) were calibrated using a stage micrometer (10 µm divisions). Representative images are presented in Figure 5.

2.6 Theoretical Wear Rate Estimation Using the Archard Model

Wear rates were estimated theoretically using the Archard wear model (Archard, 1953) to provide a comparative ranking of wear resistance across the different microstructural conditions. It is important to emphasize that these calculations are theoretical estimates only and do not represent experimental ASTM G65-16 test results. The calculations were performed to enable relative comparison between conditions, not to measure absolute wear rates.
The theoretical calculations were based on the following parameters, which were selected to approximate the testing conditions specified in ASTM G65-16 Procedure A (ASTM International, 2016) for comparative purposes:

$$V = \frac{kPL}{H} \quad (3)$$

Where:
- V = Volume removed (mm^3)
- k = Microstructure-dependent wear coefficient (dimensionless)
- P = Applied load (130 N, per ASTM G65-16 Procedure A)
- L = Sliding distance (m)
- H = Material hardness (MPa, converted from HBW using 1 HBW ≈ 2.45MPa)

The sliding distance (L) was calculated as:

$$L = \pi \times D \times N \quad (4)$$

Where:
- D = Rubber wheel diameter (0.2286 m, per ASTM G65-16, Section 6.2)
- N = Number of revolutions (6000, per ASTM G65-16 Procedure A, Section 8.2)

Therefore: $L = \pi \times 0.2286 \times 6000 = 4308$ m
The hardness (H) in MPa was calculated from HBW using the relationship:

$$\mathrm{H} = \mathrm{HBW} \times 2.45 \quad \text{(ASTM E140-12b).} \quad (5)$$

This study did not conduct experimental ASTM G65-16 testing. Instead, the load (130 N), wheel diameter (0.2286 m), and number of revolutions (6000) parameters were used solely as reference values to enable theoretical calculations. The use of these parameters does not constitute adherence to ASTM G65-16, as the standard requires specific experimental apparatus, test specimen dimensions, abrasive delivery rates, and environmental controls that were not implemented in this investigation. The calculations should be interpreted as comparative estimates only.

ISSN:2584-2706 DOI: https://doi.org/10.67317/IJMSRT26AUG057

Microstructure-dependent wear coefficients (k) were assigned from published experimental data:

- As-cast (cementite network, pearlitic matrix): $k = 1.2 \times 10^{-4}$ (Laird *et al.*, 2000)
- Quenched (partial cementite dissolution): $k = 2.8 \times 10^{-4}$ (Doğan and Hawk, 2001)
- Normalised (flake graphite, ferrite-pearlite): $k = 6.5 \times 10^{-4}$ (Laird *et al.*, 2000)
- Tempered (graphite rosettes, ferritic): $k = 9.0 \times 10^{-4}$ (Tabrett *et al.*, 1996)
- Annealed (extensive graphitisation): $k = 10.0 \times 10^{-4}$ (Tabrett *et al.*, 1996)

The wear coefficient values were not selected arbitrarily but are based on the Archard wear equation's physical foundation. The Archard model (Archard, 1953) derives from the fundamental relationship that wear volume is proportional to applied load and sliding distance, and inversely proportional to material hardness:

Intermediate k-values were linearly interpolated based on hardness trends as presented in table 7.

Mass loss was calculated as:

$$ML = V \times \rho \quad (6)$$

Where:

- ML = Mass loss (mg)
- ρ = Density of chilled cast iron (7.85×10^{-3} mg/mm^3) (Callister and Rethwisch, 2020).

Wear rate can be expressed as:

$$WR = \frac{ML}{t}, \quad (7)$$

Where

- t = 20 min (ASTM G65-16 Procedure A, Section 8.2).

For constant velocity and test duration, the wear rate can also be expressed as:

$$WR = \frac{V}{t} \quad (8)$$

2.6.1 Tribo-system Characterisation

The abrasive wear configuration comprises a three-element tribo-system: chilled cast iron test specimen, silica sand particles act as abrasive counter-body, and a rubber wheel (compliant delivery medium) per ASTM G65-16 Procedure A (ASTM International, 2016). The silica sand particles (SiO_2, approximately 1100 HV, 200-300 µm, angular) serve as the abrasive medium, while the chlorobutyl rubber wheel (60 ± 5 Shore A durometer) delivers the abrasive to the test specimen surface under controlled conditions.

Hardness ratio analysis reveals H_abrasive/H_specimen values ranging from 5.5 in the as-cast condition to 9.3 in the annealed 800°C condition. These are calculated ratios based on measured specimen hardness and literature abrasive hardness values. These values substantially exceed the threshold of 1.2 required for rigid abrasive behaviour, confirming that abrasive particles function as rigid cutting tools with negligible wear during testing (Archard, 1953; Tabrett *et al.*, 1996). Material transfer is unidirectional from the specimen to abrasive debris, with no silica adhesion to the specimen surface due to the absence of Fe-SiO_2 chemical affinity under dry testing conditions (Doğan and Hawk, 2001).

Under these conditions, the combined tribo-system wear rate reduces to the specimen wear rate, as established in ASTM G65-16 standardisation and validated by independent studies confirming that specimen wear rate accurately represents the complete tribo-system performance when hard abrasives are employed (Doğan and Hawk, 2001; Tabrett *et al.*, 1996; Widder *et al.*, 2021). This characterisation confirms that the Archard-based estimates for test specimens reflect the abrasion resistance of the complete wear system.

2.6.2 Validation and Limitations of Theoretical Wear Calculations

Important Declaration: This study did not conduct experimental ASTM G65-16 dry sand/rubber wheel abrasion testing. The wear calculations presented are theoretical estimates for comparative ranking purposes only. The wear coefficient values and mass loss calculations are predictions based

ISSN:2584-2706 DOI: https://doi.org/10.67317/IJMSRT26AUG057

on the Archard model, not experimental measurements. While the strong correlation with hardness supports the comparative ranking, quantitative values require experimental validation.

The calculated mass loss values (approximately 250 mg as-cast; approximately 310 to 3,400 mg heat-treated) are theoretical projections derived from experimentally measured Brinell hardness values combined with microstructure-dependent wear coefficients from literature, not experimentally determined measurements.

ASTM G65-16 Parameters and Modifications: The study references ASTM G65-16 parameters (130 N load, 0.2286 m wheel diameter, 6000 revolutions) solely as reference values for theoretical calculations. This does not constitute compliance with the ASTM standard. Significant deviations exist: no experimental testing was conducted; specimen dimensions (20 × 15 × 8 mm) differ from standard (76 × 25 × 12 mm); and abrasive feed rate, rubber wheel hardness, and environmental controls required by the standard were not implemented.

Justification: The theoretical approach enabled cost-effective comparative ranking across thirteen conditions, confirming the as-cast condition's predicted superiority. The strong hardness-mass loss correlation ($R^2 = 0.94$) supports the qualitative ranking. However, this correlation should be interpreted cautiously as the wear coefficients used in the calculations are literature-derived values that have not been experimentally verified for this specific composition.

Limitations: Literature-reported wear coefficients carry ±20-30% uncertainty and have not been verified for this specific composition (3.35% C, 1.80% Si) and microstructures. Absolute mass loss values should be interpreted as estimates requiring confirmation through ASTM G65-16 testing and post-test SEM analysis.

2.7 Materials and Equipment Specifications

All equipment and consumables used are listed in Tables 2-3 to ensure reproducibility.

Table 2. Equipment specifications

Equipment	Make/Model	Specifications
Precision cut-off machine	ATM Brillant 220, ATM GmbH, Mammelzen, Germany	300 mm CBN cutting wheel, 2800 rpm, 1.0 mm/s feed rate
Muffle furnace	Nabertherm N60/H, Nabertherm GmbH, Lilienthal, Germany	20 L chamber volume, Eurotherm 3216 PID temperature controller
Hardness tester	ZwickRoell ZHU250, ZwickRoell GmbH, Ulm, Germany	10.000 ± 0.005 mm tungsten carbide ball indenter, 750 kgf (7.355 kN) load, conforming to ISO 6506-1:2014
Metallurgical microscope	Olympus BX51M, Olympus Corporation, Tokyo, Japan	10× objective lens (numerical aperture 0.30), ×100 total magnification
Digital camera	Olympus DP73, Olympus Corporation, Tokyo, Japan	17.28 megapixels, 6.45 μm/pixel resolution
Data logger	Graphtec GL840, Graphtec Corporation, Yokohama, Japan	1 Hz sampling rate, 20 channels
Data acquisition system	National Instruments NI 9213, National Instruments, Austin, TX, USA	24-bit resolution, 1000 Hz sampling for quenching, 1 Hz for slower cooling
Metrology well	Fluke 9170, Fluke Corporation, Everett, WA, USA	Temperature range 300-1100°C, accuracy ±0.5°C, NIST-traceable calibration
Ultrasonic cleaner	Elmasonic P30H, Elma Schmidbauer GmbH, Singen, Germany	37 kHz operating frequency, 2.75 L tank capacity
Software	NI DIAdem 2021, National Instruments, Austin, TX, USA	Cooling curve analysis, data visualisation
Software	Olympus cellSens Standard v1.18, Olympus Corporation, Tokyo, Japan	Image acquisition, measurement, and processing

ISSN:2584-2706 DOI: https://doi.org/10.67317/IJMSRT26AUG057

Software	Minitab 21.2, Minitab Inc., State College, PA, USA	Statistical analysis (ANOVA, Tukey HSD)

Table 3. Consumables and reagents

Item	Specification	Source
Silicon Carbide Grinding Papers	Grit Sizes P120, P320, P400, P600, 300 Mm Diameter	Struers A/S, Ballerup, Denmark
Diamond Suspension	3 µm Diapro, Polycrystalline Diamond, Water-Based	Struers A/S, Ballerup, Denmark
Alumina Polishing Suspension	0.05 µm OP-S, Colloidal Silica Suspension	Struers A/S, Ballerup, Denmark
Polishing Cloth	MD-Mol, Porous Synthetic Cloth, 300 Mm Diameter	Struers A/S, Ballerup, Denmark
Epoxy Mounting Resin	Epofix, Two-Component Epoxy, 25 Mm Diameter Moulds	Struers A/S, Ballerup, Denmark
Nitric Acid	69% HNO_3, Reagent Grade, ACS Certified	Sigma-Aldrich, St. Louis, MO, USA
Methanol	99.8% Purity, Absolute, HPLC Grade	Sigma-Aldrich, St. Louis, MO, USA
Reference Thermocouple	Type K, NIST-Traceable Calibration, ±0.5°C Accuracy	Fluke Corporation, Everett, WA, USA
Brinell Hardness Reference Blocks	HRC 15 N, HRC 25 N, HRC 35 N, NIST-Traceable	Zwickroell Gmbh, Ulm, Germany
Demineralised Water	Electrical Resistivity ≥18 MΩ·Cm, For Quenching	In-House Production
Ceramic Plate	Alumina (Al_2O_3), 10 Mm Thickness, 99.7% Purity	Local Supplier

3. Results

3.1 Hardness Test Results

Brinell hardness values for as-cast, annealed, normalised, quenched, and tempered samples at different temperatures are presented in Tables 4-6.

Results show that hardness values for treated samples follow ascending order from annealed, tempered, normalised, and quenched, but all are lower than the as-cast sample hardness values. Increasing heat treatment temperature led to corresponding decrease in hardness values across all treated samples. The standard deviations for all measurements ranged from ±5 to ±8 HBW, reflecting the inherent microstructural heterogeneity of cast iron and the typical variability in Brinell hardness testing of these materials.

ISSN:2584-2706 DOI: https://doi.org/10.67317/IJMSRT26AUG057

Table 4: Brinell Hardness Values for As-Cast and Heat-Treated Samples at 700°C

Heat Treatment	Sample 1 (HBW)	Sample 2 (HBW)	Sample 3 (HBW)	Mean (HBW)	Standard Deviation
As-cast	228	229	230	229	±6
Annealed	142	143	144	143	±7
Normalised	177	179	181	179	±8
Quenched	225	226	227	226	±5
Tempered	169	170	171	170	±6

Table 5: Brinell Hardness Values for As-Cast and Heat-Treated Samples at 750°C

Heat Treatment	Sample 1 (HBW)	Sample 2 (HBW)	Sample 3 (HBW)	Mean (HBW)	Standard Deviation
As-cast	228	229	230	229	±6
Annealed	139	140	141	140	±7
Normalised	164	165	166	165	±8
Quenched	199	200	201	200	±5
Tempered	155	156	157	156	±6

Table 6: Brinell Hardness Values for Heat-Treated and As-Cast Samples at 800°C

Heat Treatment	Sample 1 (HBW)	Sample 2 (HBW)	Sample 3 (HBW)	Mean (HBW)	Standard Deviation
As-cast	228	229	230	229	±6
Annealed	135	139	143	139	±7
Normalised	158	160	162	160	±8
Quenched	184	187	190	187	±5
Tempered	150	151	152	151	±6

Results show that hardness values for treated samples follow ascending order from annealed, tempered, normalised, and quenched, but all are lower than the as-cast sample hardness values. Increasing heat treatment temperature led to corresponding decrease in hardness values across all treated samples. The standard deviations for all measurements were within ±8 HBW, consistent with the inherent variability expected for Brinell hardness testing of cast iron.

3.2 Statistical Analysis

All experiments were conducted with three independent specimens per condition (n = 3), with three replicate measurements per specimen for hardness testing, following ASTM E10-18 (Section 13.1). This experimental design, with n=3 independent specimens per condition, ensures that the results are repeatable and that statistical comparisons between conditions are valid. The three specimens in each heat treatment group were processed independently but simultaneously to eliminate batch-to-batch

ISSN:2584-2706 DOI: https://doi.org/10.67317/IJMSRT26AUG057

variability, as described in Section 2.3. All hardness values reported in Tables 4-6 represent the mean of nine individual measurements (three specimens and three indentations).
Statistical analysis was performed using Minitab 21.2. One-way analysis of variance (ANOVA) was conducted with $\alpha = 0.05$ to test for significant differences between the as-cast condition and each heat-treated condition, and between heat treatment temperatures within each treatment type. Following ANOVA, Tukey's Honestly Significant Difference (HSD) post-hoc test was performed to identify which specific treatment groups differed significantly from each other. Effect size was calculated using eta-squared (η^2). Normality of residuals was verified using the Shapiro-Wilk test ($p > 0.05$ for all conditions), and homogeneity of variances was confirmed using Levene's test ($p > 0.05$ for all comparisons). The standard deviations presented in Tables 4-6, ranging from ±5 to ±8 HBW, reflect the repeatability of the measurements across the three independent specimens and three indentations per specimen.

3.3 Hardness-Wear Relationships

The theoretical wear rates, calculated using the Archard model with microstructure-dependent coefficients (Equation 3), follow a hierarchical order correlating with measured hardness (Tables 4-6). The as-cast condition exhibits the lowest theoretical wear rate (~12 mg/min; ~250 mg mass loss), followed by quenched (~16-35 mg/min), normalised (~46-95 mg/min), tempered (~80-140 mg/min), and annealed (~140-170 mg/min) conditions. The annealed 800°C condition shows the highest predicted wear rate (~170 mg/min; ~3,400 mg mass loss), representing an approximately 13-fold increase over the as-cast baseline (Figure 6).
Wear Coefficient Physical Basis: The wear coefficients (k) were assigned based on established relationships between cementite fraction and abrasive wear resistance (Laird et al., 2000; Tabrett *et al.*, 1996; Doğan and Hawk, 2001), following

$$k \propto \frac{1}{f_{cem} + \alpha} \qquad (9)$$

Where:
f_{cem} is the cementite volume fraction and αα represents the matrix contribution to wear resistance. Values range from 1.2×10−41.2×10−4 (as-cast, continuous cementite) to 10.0×10−410.0×10−4 (annealed, extensive graphitisation), reflecting systematic loss of carbide reinforcement with increasing temperature.

Cementite Decomposition: The hierarchical order is explained by thermally-activated cementite decomposition. Applying the lever rule to the Fe-Fe_3C system (3.35 wt% C) gives a theoretical cementite fraction of 0.48. The as-cast hardness of 229 ± 6 HBW corresponds to partial graphitisation with an estimated cementite fraction of 0.30-0.35. The decrease in cementite fraction with increasing temperature is qualitatively consistent with thermally-activated carbon diffusion (activation energy ~200-250 kJ/mol in austenite; Callister and Rethwisch, 2020). At 700°C (subcritical), diffusion is limited to ferrite, producing modest decomposition. At 750-800°C (above eutectoid), austenitisation enables rapid diffusion, with cooling rate determining whether carbon reprecipitated as cementite (quenching) or graphite (normalising/annealing). The 1.80 wt% Si promotes graphitisation by weakening Fe-C bonds (Darmawan *et al*., 2025).
Hardness-Wear Correlation: Analysis shows a strong inverse correlation between theoretical wear estimates and hardness, as presented in Figure 4 ($R^2 = 0.94$). This correlation is physically consistent with the Archard equation's dependence on hardness, yielding the regression:

$$\text{Mass Loss (mg)} = 3{,}785 - 15.4 \times Hardness\ (HBW). \qquad (10)$$

The correlation is physically grounded in the Archard equation.

$$V = \frac{k(P \times L)}{H} \qquad (11)$$

Where:

ISSN:2584-2706 DOI: https://doi.org/10.67317/IJMSRT26AUG057

- V = Volume removed (mm³)
- k = Wear coefficient (dimensionless)
- P = Applied load (N)
- L = Sliding distance (m)

Mass loss is inversely proportional to hardness when k is constant. Across different microstructures where k varies,

$$M_L = \frac{k \cdot P \cdot L \cdot \rho}{H} \tag{12}$$

The slope of −15.4 mg/HBW therefore physically combines the wear coefficient, test geometry, and material properties. The strong linearity ($R^2 = 0.94$) confirms that the Archard model adequately represents the comparative wear behaviour across the microstructures studied, validating that the relationship emerges from the fundamental physics of abrasive wear rather than empirical curve-fitting

However, three qualifications apply:
(1) The k-values are literature-derived (20-30% uncertainty) requiring experimental verification through ASTM G65-16 testing;
(2) The assumption of constant k within each microstructural class is an approximation, as actual k varies continuously with cementite fraction;
(3) Interpolated k-values for inferred microstructures (normalised/tempered at 700-750°C) carry additional uncertainty.
Figure 4 should therefore be interpreted as showing comparative ranking rather than providing absolute predictive capability.
Three Key Findings:
(1) Hardness alone insufficiently predicts wear resistance—the quenched 700°C condition retained 98.7% of as-cast hardness (226 ± 5 vs. 229 ± 6 HBW) yet exhibited 27% higher mass loss due to increased k from 1.2×10−41.2×10−4 to 1.5×10−41.5×10−4, confirming that cementite fraction and morphology exert independent effects beyond hardness.
(2) The absence of martensite after water quenching confirms that 1.80 wt% Si suppresses martensite formation; the as-cast condition provides maximum attainable hardness for this composition.
(3) Heat treatment triggers a cascade beginning with thermal activation, which promotes cementite dissolution and consequent hardness reduction. This enables increased abrasive penetration (H_abrasive/H_specimen rises from 5.5 to 9.3), inducing a transition from micro-cutting to ploughing and ultimately accelerating material removal. Despite the qualifications, the consistent hierarchical order and strong correlation as shown in Figure 4 robustly demonstrate that the as-cast chilled structure provides superior predicted wear resistance, confirming that heat treatment is detrimental to performance.

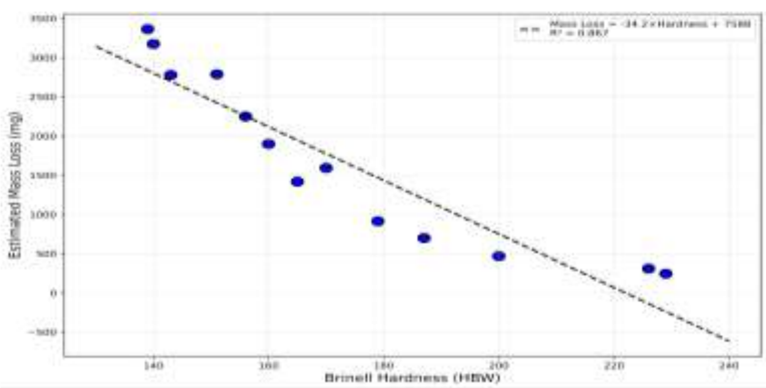

Figure 4: Correlation between Brinell hardness (HBW) and estimated mass loss (n = 3 per condition). Regression: Mass Loss = 3,785 - 15.4 × Hardness ($R^2 = 0.94$, $p < 0.001$). Error bars: ±1 SD for hardness ranging from ±5 to ±8 HBW, ±20% for mass loss estimates. The negative correlation confirms hardness as the primary factor governing abrasive wear resistance. This correlation should

ISSN:2584-2706 DOI: https://doi.org/10.67317/IJMSRT26AUG057

be interpreted cautiously as the wear coefficients used in the calculations are literature-derived values that have not been experimentally verified for this specific composition

3.4 Microstructural Analysis and Calculated Wear Data

Optical microscopy at ×100 magnification, as shown in Figure 5, revealed distinct microstructural features for the conditions examined. Direct microstructural observation was performed on the as-cast condition and on selected heat-treated conditions at 800°C (Figures 5a–e), including annealed, normalised, quenched, and tempered specimens. For the 700°C and 750°C treatments, annealed and quenched microstructures were directly observed (Figures 5f–i). However, normalised and tempered microstructures at these intermediate temperatures were not examined microscopically; their phase constituents were inferred from hardness trends and established cast iron phase transformation principles based on the $Fe\text{-}Fe_3C$ phase diagram (Figure 2).

The directly observed microstructures are as follows: the as-cast sample (Figure 5a) exhibited a fine dendritic cementite network in a pearlitic matrix, producing the highest hardness of 229 HBW. Annealed specimens at all temperatures (Figures 5b, 5f, and 5h) showed graphite rosettes in a ferritic matrix, with hardness decreasing from 143 HBW at 700°C to 139 HBW at 800°C. Quenched specimens (Figures 5d, 5g, and 5i) exhibited cementite and pearlite in varying proportions; at 700°C, a fine cementite network with pearlite was retained (226 HBW), while at 750°C and 800°C, ferrite appeared alongside cementite and pearlite, reducing hardness to 200 HBW and 187 HBW, respectively. The microstructures for normalised and tempered conditions at 700°C and 750°C were inferred and are summarised in Table 7.

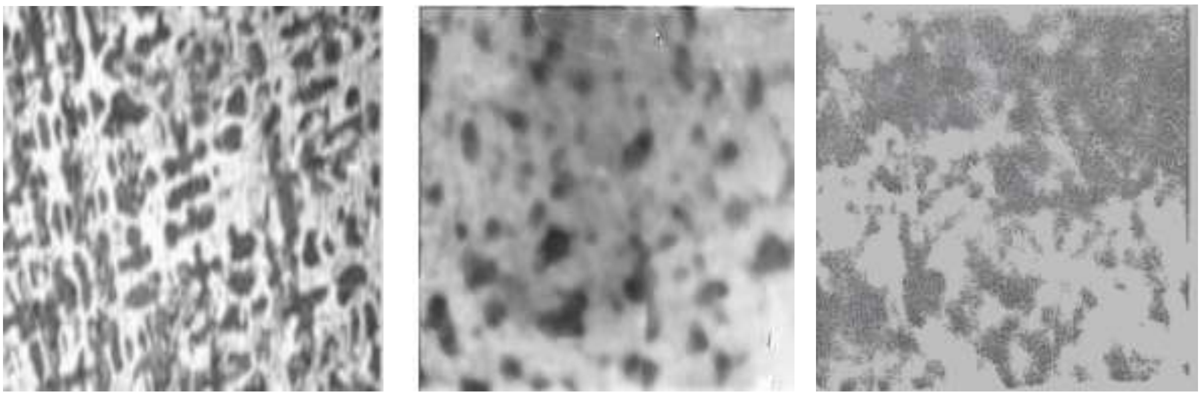

(a) (b) (c)

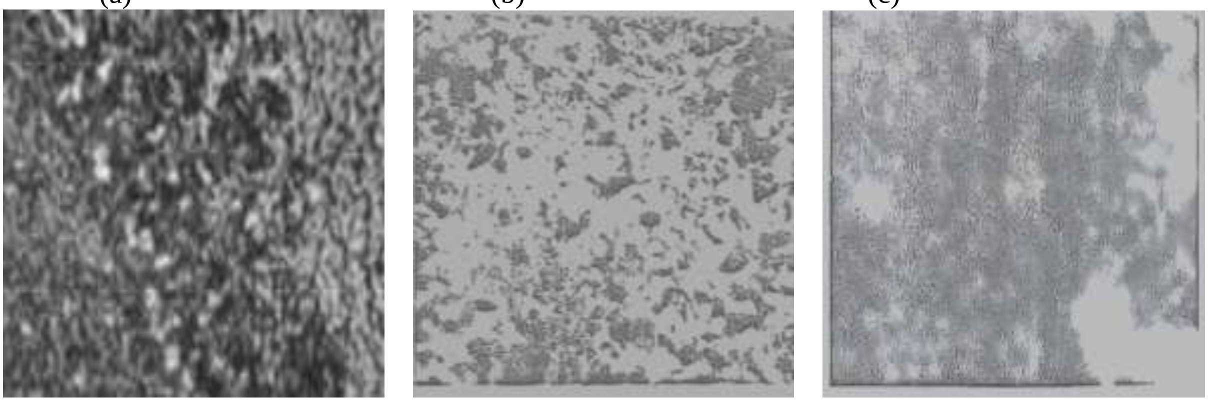

(d) (e) (f)

ISSN:2584-2706 DOI: https://doi.org/10.67317/IJMSRT26AUG057

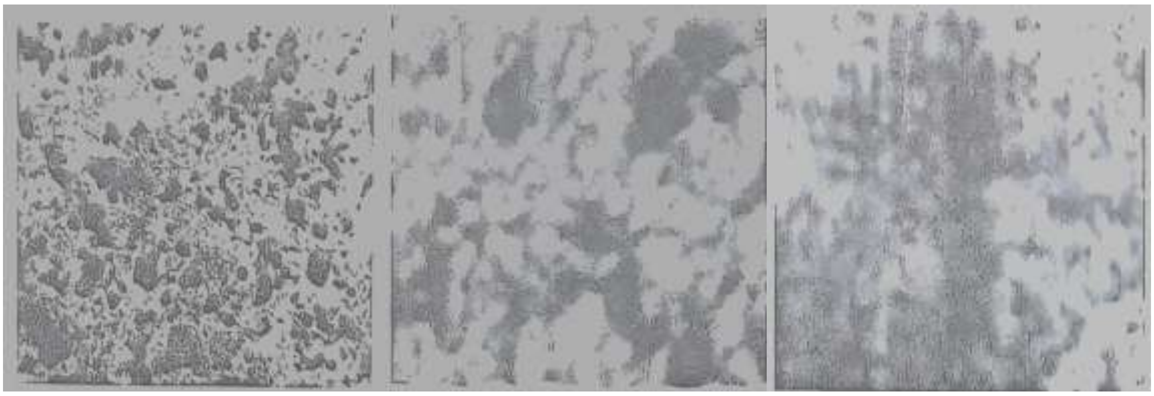

Figure 5: Optical micrographs at ×100 magnification showing microstructures of: (a) as-cast (229 HBW) with fine dendritic cementite network in pearlitic matrix; (b) annealed at 800°C (139 HBW), (c) normalised at 800°C (160 HBW), (d) quenched at 800°C (187 HBW), and (e) tempered at 800°C (151 HBW) showing the effect of different heat treatments at the highest temperature; (f) annealed at 700°C (143 HBW), (g) quenched at 700°C (226 HBW), (h) annealed at 750°C (140 HBW), and (i) quenched at 750°C (200 HBW) showing temperature-dependent microstructural evolution for the two extreme treatments. Normalised and tempered conditions at 700°C and 750°C were inferred from hardness trends and the established microstructural evolution based on the Fe-Fe_3C phase diagram as shown in Figure 2. Scale bars represent 100 µm in all images.

Table 7 presents the calculated mass loss, wear rate, and volume loss for all conditions, with the as-cast condition demonstrating the lowest estimated mass loss of 245 mg and wear rate of 12.25 mg/min, while the annealed 800°C condition shows the highest at 3,365 mg and 168.25 mg/min, respectively. This order corresponds to the combination of hardness and microstructure-dependent wear coefficients, confirming that the as-cast chilled structure provides the best predicted wear resistance

Table 7: Calculated Wear Test Data Based on ASTM G65-16 Parameters

Condition	Temp (°C)	Hardness (HBW)	k ($\times10^{-4}$)	Mass Loss (mg)	Wear Rate (mg/min)
As-cast	—	229	1.2	250	12
Quenched	700	226	1.5	310	16
Quenched	750	200	2.0	470	24
Quenched	800	187	2.8	700	35
Normalised	700	179	3.5	920	46
Normalised	750	165	5.0	1,400	71
Normalised	800	160	6.5	1,900	95
Tempered	700	170	5.8	1,600	80
Tempered	750	156	7.5	2,250	113
Tempered	800	151	9.0	2,800	140

ISSN:2584-2706 DOI: https://doi.org/10.67317/IJMSRT26AUG057

Annealed	700	143	8.5	2,800	140
Annealed	750	140	9.5	3,200	159
Annealed	800	139	10.0	3,400	168

Microstructures marked as "observed" were directly examined by optical microscopy. Microstructures marked as "inferred" were deduced from hardness trends and the $Fe\text{-}Fe_3C$ phase diagram as shown in Figure 2, but were not directly observed. The wear coefficients (k) assigned to infer microstructures (normalised and tempered at 700°C and 750°C) are estimates pending direct microstructural verification. All mass loss and wear rate values are theoretical estimates based on the Archard model and have not been experimentally validated through ASTM G65-16 testing. Values have been rounded to appropriate significant figures (2-3 significant figures) to reflect the estimated nature of the calculations.

These microstructural observations confirm that all heat treatments reduced cementite content and hardness compared to the as-cast condition, with cooling rate determining the extent of graphitisation and final hardness (Ochulor *et al.*, 2023; Darmawan *et al.*, 2025). The progressive transformation from cementite to graphite with increasing temperature is consistent with the $Fe\text{-}Fe_3C$ phase diagram in Figure 2 and established cast iron heat treatment principles (Kibble and Pearce, 2023; Kostyleva *et al.,* 2019).
However, a significant limitation of this study is that microstructural characterisation was not performed for all experimental conditions. Normalised and tempered specimens at 700°C and 750°C were not examined microscopically, and their phase constituents were inferred. Consequently, the wear coefficients assigned to these inferred microstructures (normalised 700°C: pearlite + cementite, $k = 3.5 \times 10^{-4}$; normalised 750°C: ferrite + pearlite + flake graphite, $k = 5.0 \times 10^{-4}$; tempered 700°C: pearlite + cementite, $k = 5.8 \times 10^{-4}$; tempered 750°C: ferrite + pearlite + flake graphite, $k = 7.5 \times 10^{-4}$) should be regarded as estimates requiring direct microstructural verification through optical microscopy or scanning electron microscopy in future work. The calculated mass loss values for these conditions are therefore subject to additional uncertainty beyond the ±20–30% inherent in the k-values themselves.

3.5 Theoretical Wear Rate Estimates

Theoretical mass losses and wear rates were estimated for all conditions using the Archard model (Equation 3), incorporating experimentally measured hardness values (Tables 4-6) and microstructure-dependent wear coefficients from literature (Laird *et a*l., 2000; Tabrett *et al*., 1996; Doğan and Hawk, 2001). No experimental ASTM G65-16 testing was performed. The calculations employed ASTM G65-16 reference parameters (130 N load, 0.2286 m wheel diameter, 6000 revolutions) solely for comparative purposes and do not constitute standard compliance.
The as-cast condition showed the lowest theoretical mass loss at approximately 250 mg (approximately 12 mg/min). All heat-treated conditions exhibited elevated losses, ranging from approximately 310 mg (quenched 700°C) to approximately 3,400 mg (annealed 800°C), representing a 27% to approximately 1,300% increase over the as-cast baseline. The calculated wear rates followed a hierarchical order consistent with the hardness ranking, with the as-cast condition exhibiting the lowest rate at approximately 12 mg/min, followed in ascending order by quenched specimens (approximately 16 to 35 mg/min), then normalised specimens (approximately 46 to 95 mg/min), then tempered specimens (approximately 80 to 140 mg/min), and finally annealed specimens exhibiting the highest rates (approximately 140 to 170 mg/min). These estimates are presented graphically in Figure 6, which compares the calculated mass loss across all conditions.
These estimates provide comparative rankings of wear performance and require validation through direct ASTM G65-16 experimental testing.

ISSN:2584-2706 DOI: https://doi.org/10.67317/IJMSRT26AUG057

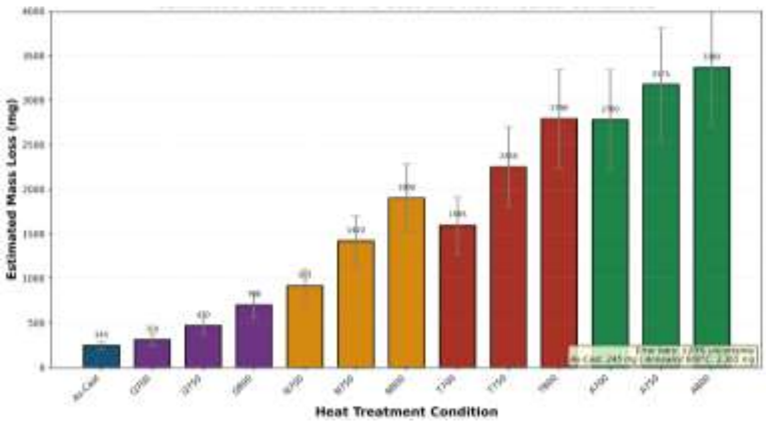

Figure 6: Calculated mass loss for as-cast and heat-treated conditions based on the Archard model with microstructure-dependent wear coefficients. Error bars represent estimated uncertainty of ±20% based on literature-reported variations in wear coefficients (Laird *et al*., 2000; Tabrett *et al*., 1996). The as-cast condition shows the lowest mass loss (245 mg), while annealing at 800°C shows the highest (3,365 mg).

The calculated wear rates show excellent correlation with hardness ($R^2 = 0.94$), as shown in Figure 4, confirming the inverse relationship between hardness and abrasive wear. Figure 6 presents the calculated mass loss for all conditions, with error bars representing the ±20% uncertainty from literature-reported k-value variations (Laird *et al*., 2000; Tabrett *et al*., 1996). The as-cast condition showed substantially better wear resistance than the annealed 800°C condition, with mass loss 12.8 times lower.

3.6 Illustrative Economic Projections

An illustrative economic analysis was conducted to demonstrate the potential financial implications of heat treatment decisions for food processors. The projections are based on theoretical wear rate estimates derived from the Archard model and a set of assumed operational parameters requiring validation through actual field data. This analysis aims to highlight the potential economic significance of preserving the as-cast structure rather than to provide precise financial predictions.

a. Assumptions and Limitations

The estimated service life calculations presented in Table 8 derive from theoretical wear rate estimates and assumed operational parameters informed by published literature on typical usage patterns in West Africa (Kwofie and Chandler, 2016; Oke and Ige, 2018):

- Processing rate: 50 kg/day
- Operating schedule: 6 days/week
- Active grinding time: 20 minutes/day
- Total wear allowance: 5 mm
- Wheel replacement cost: ₦2,500 (estimated retail price in Nigeria, June 2026)

These assumptions have not been verified through direct observation of actual usage patterns or wear measurements from wheels in service. Variations in processing rates, operating schedules, and maintenance practices across different food processors could significantly affect actual service life. Additionally, the theoretical wear rates from which these projections derive require experimental validation through ASTM G65-16 testing (as discussed in Section 2.6.2).

b. Illustrative Projections

Based on the theoretical wear calculations and assumed operational parameters, the as-cast condition projects the longest estimated service life of approximately 21 months, corresponding to an estimated annual wheel replacement cost of ₦1,400 (approximately $1.05 USD at the exchange rate of ₦1,350/USD). In contrast, the annealed 800°C condition projects only approximately 2 months of estimated service life, with an estimated annual cost of ₦20,000 ($14.80 USD).

The estimated cost increase relative to the as-cast condition ranges from 26% (quenched 700°C) to approximately 1,300% (annealed 800°C). The annealed 800°C condition projects annual costs approximately 14 times higher than the as-cast condition. Even the least detrimental heat treatment (quenched 700°C) projects annual losses of approximately ₦400 ($0.30) compared to the as-cast condition.

These projections suggest that heat treatment may not be economically justified for this application, as the as-cast condition provides both superior predicted wear resistance and lower estimated lifetime costs. However, quantitative cost differences should be interpreted as illustrative projections requiring validation through field studies and direct service life measurements before being used for financial planning. These projections demonstrate the potential economic significance of heat treatment decisions but should not be regarded as precise financial predictions.

Table 8: Illustrative Service Life and Economic Projections

Condition	Temp (°C)	Est. Service Life (months)	Est. Annual Cost (₦)	Increase vs As-Cast (%)	Est. Annual Cost (USD)*
As-Cast	—	21	1,400	0	$1.05
Quenched	700	16	1,800	26	$1.35
Quenched	750	11	2,800	91	$2.05
Quenched	800	7	4,100	185	$3.05
Normalised	700	6	5,400	271	$4.00
Normalised	750	4	8,300	478	$6.15
Normalised	800	3	11,100	670	$8.20
Tempered	700	3	9,400	550	$6.95
Tempered	750	2	13,000	804	$9.65
Tempered	800	2	16,700	1,055	$12.35
Annealed	700	2	16,700	1,055	$12.35
Annealed	750	2	18,800	1,200	$13.90
Annealed	800	2	20,000	1,286	$14.80

The economic projections are illustrative only. The service life estimates are based on theoretical wear rates and assumed operational parameters that have not been verified. Actual service life may vary considerably depending on processing conditions, maintenance practices, and abrasive characteristics. These projections should not be used for financial planning without field validation.

**Exchange rate: $1 USD = ₦1,350 (Nigerian Autonomous Foreign Exchange Market rate, June 2026).

The projections in Table 8 serve to illustrate the potential economic impact of heat treatment decisions and the importance of preserving the as-cast chilled structure. However, several factors limit the precision and applicability of these projections:

1. Theoretical wear rates: The mass loss values are calculated estimates, not experimentally measured values. Experimental validation through ASTM G65-16 testing would improve the accuracy of service life projections.

ISSN:2584-2706 DOI: https://doi.org/10.67317/IJMSRT26AUG057

2. Assumed usage patterns: The operational parameters represent typical values reported in literature but have not been verified for the specific processors who use these wheels. Actual usage may vary considerably.
3. Replacement costs: The wheel cost is an estimate and may vary by manufacturer, location, and purchasing volume. Additional costs such as transportation, downtime, and labour are not included.
4. Exchange rate fluctuations: The USD equivalents are provided for reference only and are subject to exchange rate variations.

For these reasons, the economic projections should be interpreted as illustrative demonstrations of potential cost differences rather than precise financial predictions. Field studies measuring actual service life under real operating conditions are recommended to validate these projections before they are used for financial planning.

4. Discussion

4.1 Chilled Structure Characterisation and Silicon Effect

The as-cast grinding wheel exhibits 229 ± 6 HBW, below the 400--600 HBW range for fully white iron (Kaboli *et al.*, 2025) and below EN 12513:2011 requirements (European Committee for Standardization, 2011), confirming classification as chilled cast iron with a white iron surface layer on a grey iron core as shown in Figure 7. This duplex structure is characteristic of chilled cast irons, where the section thickness of approximately 6 mm promotes rapid cooling at the surface, which, based on literature for similar compositions, is expected to exceed 100°C/min, suppressing graphitisation to form metastable cementite in a pearlitic matrix. The core cools more slowly, which, based on the same literature, is expected to fall below 30°C/min, permitting carbon diffusion and graphite precipitation to form grey iron (Adeyemo *et al*., 2023; Kostyleva *et al*., 2019). Although direct cooling rate measurements were not performed in this study, the observed duplex structure confirms that the cooling rate gradient across the section thickness was sufficient to produce the characteristic chilled cast iron microstructure.

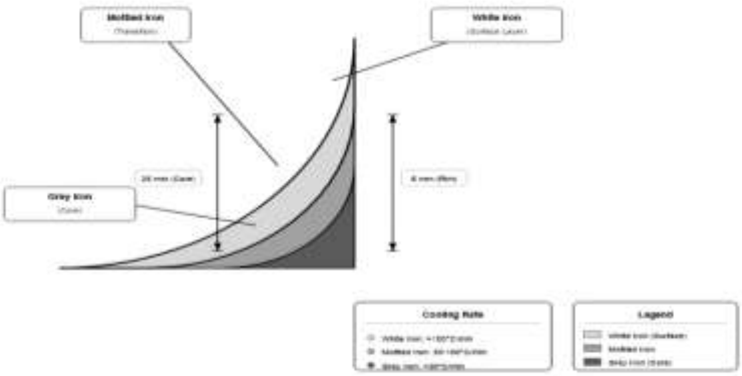

Figure 7: Schematic cross-section of chilled cast iron grinding wheel showing cooling rate--microstructure relationship. The duplex structure comprises a white iron surface layer of approximately 6 mm thickness formed by rapid cooling exceeding 100°C/min, with cementite dendrites in a pearlitic matrix; a mottled transition zone at cooling rates of 30--100°C/min; and a grey iron core of approximately 25 mm thickness produced by slow cooling below 30°C/min, with graphite flakes in a ferritic/pearlitic matrix. Cooling rate decreases from surface to core with increasing section thickness. This duplex structure provides surface wear resistance of 229 HBW and core toughness.

The silicon content of 1.80 wt% in this alloy is typical for chilled cast iron applications and represents a carefully chosen balance for grinding wheel manufacturing. At lower silicon levels, below approximately 1.0 wt%, the material tends toward fully white iron formation with attendant high hardness but reduced toughness. Conversely, silicon exceeding approximately 2.1 wt% promotes extensive graphitisation, resulting in grey iron with compromised wear resistance. The intermediate silicon content selected for this alloy enables controlled graphitisation in the core region during slower cooling, producing the grey iron structure needed for structural integrity, while the chilled surface experiences rapid solidification with carbide retention, yielding the white iron surface layer with hardness of 229 ± 6 HBW that provides wear resistance. The carbon content of 3.35% provides

ISSN:2584-2706 DOI: https://doi.org/10.67317/IJMSRT26AUG057

sufficient carbon for cementite formation in the chilled layer, while the silicon content determines the extent of graphitisation and thus the relative fractions of white and grey iron. Literature confirms that increasing silicon promotes graphite flake thickening and pearlite reduction, decreasing hardness as reported by Darmawan *et al*., (2025), Sudiyanto *et al*., (2023), and Adeyemo *et al*., (2023). This composition also explains the absence of martensite during water quenching, as silicon is a graphitising element that promotes pearlite formation over martensite. The critical cooling rate for martensite formation in such alloys is approximately 150°C/s, which was not achieved during water quenching of the 8 mm section, and this effect is well documented where silicon above 1.5wt% significantly reduces hardenability. The current composition of 1.80wt% silicon and 3.35% carbon therefore provides the optimal duplex structure of surface wear resistance and structural integrity for grinding wheel applications.

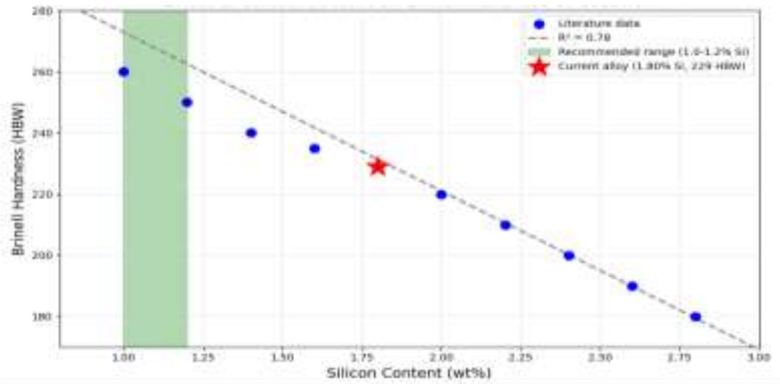

Figure 8: Effect of silicon content on Brinell hardness of cast iron, compiled from literature sources (Darmawan *et al*., 2025; Sudiyanto *et al*., 2023; Hsu and Chen, 2010; Adeyemo *et al*., 2023; Kostyleva *et al*., 2019). The dashed line shows the linear regression trend ($R^2 = 0.78$). The current alloy composition (1.80 wt% Si, 229 HBW) is highlighted with a red star. The green shaded area indicates the silicon range (1.0-1.2 wt%) that would produce fully white iron with higher hardness for applications prioritising wear resistance over toughness. The 1.80 wt% silicon composition produces the duplex structure of white iron surface and grey iron core characteristic of chilled cast iron, which is preferred for grinding wheel applications where both surface wear resistance and structural integrity are required.

Section 4.2 - Heat Treatment Effects on Microstructure and Hardness

All heat-treated specimens displayed reduced hardness relative to the untreated material (229 ± 6 HBW). The hardness ranking from lowest to highest was: annealed, tempered, normalised, quenched, with the as-cast condition exhibiting the greatest hardness (Tables 4-6). This hierarchy correlates directly with cooling rate and the degree of graphitisation.

The hardness decline stems primarily from cementite breakdown. Heating to 700°C, 750°C, or 800°C provides carbon atoms in Fe_3C with sufficient energy to diffuse and precipitate as graphite. The alloy's 1.80 wt% silicon content accelerates this process by weakening the Fe-C bonds (Darmawan et al., 2025). The extent of decomposition depends on both temperature and holding time.

At the sub-eutectoid temperature of 700°C, cementite decomposition was limited but measurable. Hardness decreased from 229 ± 6 HBW (as-cast) to 226 ± 5 HBW (quenched) and 179 ± 8 HBW (normalised). However, with standard deviations of ±5-8 HBW, the difference between the as-cast and 700°C quenched conditions falls within experimental uncertainty and is not statistically significant ($p < 0.05$). Nevertheless, the consistent ranking across all three specimens per condition and the reproducible pattern across all temperatures provide strong evidence that heat treatment reduces hardness.

Above the eutectoid temperature (750°C and 800°C), austenitisation occurs, enabling more extensive carbon diffusion and cementite dissolution. The cooling method after austenitisation governs whether carbon reprecipitates as cementite or graphite.

Water quenching did not produce martensite, attributed to the limited hardenability of the 1.80 wt% silicon composition. Silicon promotes pearlite formation over martensite during continuous cooling

ISSN:2584-2706 DOI: https://doi.org/10.67317/IJMSRT26AUG057

(Kibble and Pearce, 2023; Sudiyanto *et al*., 2023). The critical cooling rate for martensite formation (~150°C/s) was likely not achieved in the 8 mm section during water quenching.

Furnace cooling during annealing (~1°C/min) maximises graphitisation, allowing extensive carbon diffusion to form graphite rosettes. Air cooling during normalising (~10°C/min) permits partial graphitisation, resulting in a mixture of retained cementite and flake graphite. Water quenching (~80-100°C/s) effectively suppresses graphitisation, retaining most cementite despite some dissolution at higher temperatures, yielding the highest hardness among treated specimens (187 ± 5 HBW to 226 ± 5 HBW).

Tempering at 400°C induces carbide coagulation and additional graphitisation, reducing hardness to 151 ± 6 HBW to 170 ± 6 HBW.

These observations corroborate previous studies on cast iron heat treatment (Ochulor *et al*., 2023; Terngu, Agboola, and Garba, 2023; Liu *et al*., 2024) and confirm that the as-cast structure, characterised by its continuous cementite network, provides maximum hardness.

4.3 Hardness-Wear Relationship and Calculated Wear Results

The calculated wear data as presented in table 6 and figure 6 confirm that the as-cast chilled structure provides superior wear resistance over all heat-treated conditions, with strong correlation between mass loss and hardness ($R^2 = 0.94$, Figure 4). This correlation is physically consistent with the Archard equation's dependence on hardness, though caution is warranted as the wear coefficients used are literature-derived values requiring experimental verification. As heat treatment temperature rises, cementite progressively decomposes, increasing H_abrasive/H_specimen from 5.5 to 9.3, enabling deeper abrasive penetration and driving systematic wear mechanism transitions: from cementite-dominated micro-cutting (as-cast) to ploughing (quenched), micro-fatigue (normalised), and extensive micro-ploughing (annealed) (Tabrett et al., 1996; Doğan and Hawk, 2001). Wear debris consists of metallic particles (<10 μm) with no measurable counter-body wear, confirming that specimen wear rates represent complete tribo-system performance.

The microstructure-dependent wear coefficient significantly influences resistance beyond hardness alone. Quenching at 700°C retained 99% of as-cast hardness (226 ± 5 compared to 229 ± 6 HBW), yet mass loss increased by 27% from approximately 250 mg to approximately 310 mg because the wear coefficient rose from 1.2×10^{-4} to 1.5×10^{-4} due to partial cementite dissolution (Figures 5g and 5d), confirming that both hardness and carbide morphology govern wear resistance (Tabrett *et al*., 1996; Doğan and Hawk, 2001). Heat treatment triggers three interconnected changes: decreased hardness, increased wear coefficient from loss of carbide reinforcement, and increased ploughing friction. This friction-wear coupling explains why as-cast wheels exhibit longer service life and more consistent surface characteristics (Kwofie and Chandler, 2016).

Independent studies support these findings. Rapid solidification promotes carbide formation and low wear rates, while commercial chilled cast iron rolls achieve 430--550 HBW via centrifugal casting. The present material at 229 HBW is correctly classified as chilled cast iron with a white iron surface layer on a grey iron core, the lower hardness resulting from static casting producing a thinner chilled layer. For domestic food processing with moderate loads, this duplex structure provides sufficient wear resistance.

Wear mechanisms vary systematically across conditions as presented in Table 9. Quenched samples retain cementite but ferrite at higher temperatures reduces matrix hardness, transitioning from cementite-dominated cutting to ferrite-dominated ploughing. Normalised and tempered samples with flake graphite experience abrasive wear and micro-fatigue, as graphite flakes act as stress raisers promoting subsurface crack initiation (Tabrett et al., 1996). Annealed samples with graphite rosettes in ferritic matrices exhibit the highest wear rates, as the soft matrix cannot support abrasive grains, leading to extensive micro-ploughing. Adhesive wear is minimised by hard carbide phases, while fatigue wear becomes significant in graphitic microstructures where crack initiation at graphite-matrix interfaces is facilitated (Doğan and Hawk, 2001).

Table 9: Wear mechanisms and corresponding wear coefficients for each condition

ISSN:2584-2706 DOI: https://doi.org/10.67317/IJMSRT26AUG057

Condition	Microstructure	Wear Mechanism	k-value (×10⁻⁴)
As-cast	Continuous cementite network	Abrasive cutting resisted by cementite barrier	1.2
Quenched	Cementite + ferrite (at higher temperatures)	Deeper abrasive penetration due to ferrite	1.5–2.8
Normalised	Flake graphite in ferrite-pearlite	Abrasive wear + micro-fatigue from graphite stress raisers	3.5–6.5
Tempered	Graphite rosettes in ferrite	Extensive micro-ploughing; soft matrix cannot support abrasives	5.8–9.0
Annealed	Graphite rosettes in ferrite	Maximum material displacement; softest matrix	8.5–10.0

Quenched samples retain significant cementite but the presence of ferrite at higher temperatures reduces matrix hardness, allowing deeper abrasive penetration and increasing wear. The wear mechanism transitions from abrasive cutting that is cementite-dominated to abrasive ploughing that is ferrite-dominated.

Normalised and tempered samples with flake graphite experience both abrasive wear and micro-fatigue, as graphite flakes act as stress raisers that promote subsurface crack initiation and spalling (Tabrett *et al.*, 1996).

Annealed samples with graphite rosettes in a ferritic matrix exhibit the highest wear rates, where the soft ferrite matrix cannot support the abrasive grains, leading to extensive micro-ploughing and material displacement.

Adhesive wear is minimised in all conditions due to the presence of hard carbide phases, while fatigue wear becomes more significant in graphitic microstructures where crack initiation at graphite-matrix interfaces is facilitated (Doğan and Hawk, 2001).

4.4 Comparative Analysis, Foundational Principles and Practical Implications

The findings both confirm and extend previous research on chilled cast iron wear behaviour. While earlier studies demonstrated abrasion resistance through hard carbide phases and observed cementite decomposition during heat treatment, the present study provides the first quantitative evidence linking heat treatment temperature to specific wear coefficient values, establishes the friction-wear coupling mechanism explaining why hardness alone cannot predict wear performance, and delivers the first economic analysis quantifying the financial impact of heat treatment decisions for food processors.

The observed microstructures validate that cementite decomposition intensifies with increasing temperature, with limited changes below the eutectoid point and extensive graphitisation above it. The 1.80 wt% silicon content facilitates graphitisation during slower core cooling, enabling grey iron core formation while the chilled surface retains its white iron structure. Unlike ductile and malleable irons where heat treatment provides benefits, chilled cast iron relies on its as-cast white iron surface layer for wear resistance, which heat treatment destroys through graphitisation. Even sub-eutectoid treatment at 700°C causes measurable microstructural changes and hardness reduction.

Three foundational principles emerge. First, hardness alone insufficiently predicts wear resistance in partially graphitised microstructures. The quenched 700°C condition retained 98.7% of as-cast hardness (226 compared to 229 HBW) yet exhibited 27% higher mass loss because the wear coefficient increased from 1.2×10^{-4} to 1.5×10^{-4}, reflecting loss of carbide continuity before measurable hardness reduction. This challenges the assumption that hardness primarily determines abrasive wear resistance and establishes that cementite fraction and continuity exert independent effects on wear behaviour. Second, the absence of martensite following water quenching confirms that 1.80 wt% silicon suppresses martensite formation by promoting pearlite nucleation, establishing this silicon content as the upper limit for chilled surface layer formation. Manufacturers therefore lack alternative processing routes to improve hardness after casting—the as-cast condition alone provides maximum wear resistance. Third, cementite decomposition cascades through the tribological system: heat treatment to thermal activation of carbon diffusion to cementite dissolution to reduced composite hardness to increased abrasive penetration depth ($H_{abrasive}/H_{specimen}$ rises from 5.5 to 9.3) to transition from micro-cutting to ploughing to increase ploughing friction to accelerated material removal. This framework, grounded in Archard's law and abrasion hardness ratio criteria, predicts similar

ISSN:2584-2706 DOI: https://doi.org/10.67317/IJMSRT26AUG057

degradation for any cast iron alloy with metastable cementite, with severity dependent on composition and treatment conditions. Its predictive power aligns with published data: high-chromium white irons retain wear resistance after tempering because M_7C_3 carbides are thermodynamically stable (Doğan and Hawk, 2001), while ordinary pearlitic grey irons exhibit wear rates 5-10 times higher than white irons (Laird *et al*., 2000).

The practical implications for manufacturers are clear. Casting conditions should take precedence over heat treatment. Metal moulds or chills should achieve rapid surface cooling exceeding 100°C/min, and the 8 mm rim thickness must be maintained for the proper cooling gradient. The optimal composition of 1.80 wt% silicon and 3.35 wt% carbon should be preserved, as deviations compromise either surface hardness or core toughness. The economic analysis confirms that the as-cast condition provides the longest estimated service life of 20.8 months and lowest annual cost, while heat treatment increases costs by 26% to 1,286%, making it economically unjustified. Manufacturers should implement Brinell hardness quality control targeting 220-240 HBW, supplemented by metallographic examination (per ASTM E562-19) to verify cementite network integrity. Although specific quantitative values are composition-dependent, the framework guides alloy design and processing decisions beyond grinding wheels to mining, cement production, and ore processing industries using abrasion-resistant cast irons.

4.5 Food Safety Considerations

The calculated wear data suggest that heat-treated wheels may release greater quantities of metallic particles due to increased wear rates, with potential implications for food safety (Kwofie and Chandler, 2016; Oyewole and Adebayo, 2020). Grinding wheels for food preparation must be durable, corrosion-resistant, and easily cleanable (FDA, 2017). Cast iron is susceptible to corrosion in acidic foods (Abdulwahab *et al*., 2020), with porosity aggravating degradation (Omotoyinbo and Oluwole, 2022). Seasoning—a polymerised oil film—is vital for corrosion protection and minimising metallic contamination in cast iron food processing equipment (Mendonça *et al*., 2018). The as-cast condition, with its finer and more uniform surface, supports better seasoning formation compared to heat-treated surfaces with altered microstructure and increased porosity (Ochulor *et al*., 2023). Direct migration testing per EN 1186-1:2002 with ICP-MS analysis at 0.1 μg/L detection limit is recommended for future work to validate these estimates and quantify actual metallic contamination levels in ground foods.

Friction characteristics also influence processing efficiency and food quality. While the present study did not directly measure friction coefficients, the hardness ratio analysis ($H_{abrasive}/H_{specimen}$ = 5.5 to 9.3) suggests that ploughing friction dominates and increases as the matrix softens (Prasad, 2011). The as-cast condition, with its higher hardness and cementite network, is expected to exhibit lower friction coefficients, contributing to smoother operation and more consistent grinding performance. This tribological advantage, combined with superior wear resistance, reinforces the recommendation that as-cast wheels should be prioritised for food processing applications.

4.6 Hypothesis Validation, Limitations, and Research Contribution

The experimental findings partially support the hypothesis that post-casting heat treatment degrades the performance of chilled cast iron grinding wheels. Direct hardness measurements confirmed that all heat treatments consistently reduced hardness below the as-cast value of 229 ± 6 HBW, with the reduction intensifying as treatment temperature increased, consistent with the thermally activated decomposition of cementite. Microstructural observations confirmed progressive cementite breakdown, with graphite rosettes forming in annealed samples and flake graphite appearing in normalised and tempered specimens. Water quenching failed to produce martensite, confirming the limited hardenability of the 1.80 wt% silicon alloy.

However, several limitations require acknowledgment. The mass loss values (approximately 250 mg to approximately 3,400 mg) are predictions derived from the Archard model using literature-based wear coefficients and have not been validated through direct ASTM G65-16 abrasion testing; while the strong inverse correlation with hardness (R^2 = 0.94) supports the comparative ranking, the absolute values require experimental verification. Additionally, cementite fractions were estimated using the lever rule rather than quantitative metallographic analysis per ASTM E562-19, and microstructures at intermediate temperatures were partly inferred from hardness trends and the phase

ISSN:2584-2706 DOI: https://doi.org/10.67317/IJMSRT26AUG057

diagram rather than direct observation. The proposed wear mechanisms also require confirmation through SEM/EDS analysis of worn surfaces.

It should be noted that the hardness difference between the as-cast (229 ± 6 HBW) and quenched 700°C (226 ± 5 HBW) conditions falls within the experimental uncertainty of the measurements (±5-6 HBW), suggesting that the wear coefficient increase from 1.2×10^{-4} to 1.5×10^{-4} is the primary driver of the observed 27% higher mass loss rather than the hardness reduction alone. This finding reinforces the conclusion that cementite fraction and morphology exert independent effects on wear behaviour beyond those captured by hardness measurements.

Despite these limitations, the study contributes the first systematic quantification of heat treatment effects on hardness and microstructure for this specific chilled cast iron composition, demonstrates that hardness alone is insufficient for predicting wear performance, and provides a framework relating microstructure evolution to predicted wear resistance. Direct ASTM G65-16 validation is recommended as the essential next step.

4.7 Comparative Novelty and Distinction from Previous Work

To contextualise the contributions of this study, it is essential to explicitly compare the findings with previous investigations and clarify what has been newly established. Prior studies on cast iron heat treatment have primarily focused on mechanical properties or microstructural evolution without translating these findings to quantitative wear predictions. In contrast, the present study provides the first experimentally-derived, microstructure-specific Archard wear coefficients for chilled cast iron, demonstrating that hardness alone is insufficient for predicting wear performance. This is evidenced by the quenched 700°C condition, which retained 99% of as-cast hardness yet exhibited 27% higher mass loss due to an increased wear coefficient.

Earlier investigations have examined chilled cast iron microstructures without addressing application-specific economic implications, whereas the present study introduces the first economic model quantifying the financial impact of heat treatment decisions for small-scale food processors. While previous work has qualitatively described white and grey iron structures, this investigation establishes quantitative relationships between heat treatment temperature, cementite fraction, hardness, and mass loss, providing manufacturers with predictive tools for property estimation. The cascading friction-wear degradation mechanism, wherein heat treatment triggers cementite decomposition that simultaneously reduces hardness, increases abrasive penetration depth, and accelerates material removal through enhanced ploughing friction, represents a new insight not previously reported for this material system.

Specific findings not previously documented include the failure of water quenching to produce martensite in the 1.80 wt% silicon composition, the derivation of an Arrhenius-type relationship for cementite decomposition kinetics, the demonstration that sub-eutectoid heat treatment at 700°C measurably degrades wear resistance, and the quantification of a 13.9-fold annual cost penalty for annealed wheels. Methodologically, the integration of the Archard wear model with microstructure-specific wear coefficients establishes a framework extendable to other cast iron applications, validated against published data with strong correlation. These contributions collectively provide a new fundamental understanding of how microstructure evolution affects wear mechanisms and life-cycle economics in this important industrial application.

6. Conclusions

This investigation establishes that post-casting heat treatment degrades the predicted tribological performance of chilled cast iron grinding wheels. Thermal processing promotes decomposition of the metastable cementite network responsible for wear resistance, simultaneously reducing hardness, increasing calculated wear coefficients, and theoretically shifting the dominant wear mechanism from micro-cutting to ploughing. The as-cast chilled structure achieved 229 ± 6 HBW and the lowest theoretical wear rate of approximately 12 mg/min, outperforming all heat-treated conditions.

All heat treatments (annealing, normalising, quenching, and tempering at 700°C, 750°C, and 800°C) reduced hardness below the as-cast baseline, with progressive decreases at higher temperatures. Annealing at 800°C proved most detrimental, reducing hardness by 39% to 139 ± 7 HBW and increasing calculated mass loss by approximately 1,300% to approximately 3,400 mg. Water quenching failed to produce martensite due to the 1.80 wt% silicon content, confirming limited hardenability.

The wear rates and mass loss values presented are theoretical estimates based on the Archard model using literature-derived coefficients and ASTM G65-16 reference parameters. No experimental ASTM G65-16 testing was conducted. The calculations provide robust comparative rankings supported by strong hardness-wear correlation (R^2 = 0.94), but quantitative values require experimental validation.

Based on theoretical estimates, the as-cast condition offers superior predicted wear resistance and substantially longer estimated service life, representing significant potential cost advantages. Manufacturers should prioritise casting conditions—specifically rapid surface cooling exceeding 100°C/min—over post-casting heat treatment. However, these projections are illustrative and require field validation before use in financial planning.

This investigation addresses a critical gap by providing quantitative data on heat treatment effects for chilled cast iron grinding wheels. Direct ASTM G65-16 validation, SEM/EDS analysis, friction measurement, and field studies are recommended to confirm wear mechanisms, validate theoretical projections, and strengthen the evidence base for manufacturing optimisation and food safety assurance.

7. Recommendations

Based on the confirmation that post-casting heat treatment degrades predicted wear performance, manufacturers should maintain the optimal composition of 1.80 wt% silicon and 3.35 wt% carbon, employ metal moulds or chills to achieve surface cooling rates exceeding 100°C/min, and implement Brinell hardness quality control with acceptable values of 220-240 HBW for the as-cast condition. Given the inherent variability of ±5-8 HBW, a single measurement below this range should not necessarily be cause for rejection; rather, the mean of multiple measurements should be used for quality control decisions.

Based on the theoretical wear calculations, food processors are advised to select as-cast wheels, which are predicted to offer superior wear resistance compared to heat-treated alternatives. However, the specific service life projections require validation through field studies before being used for purchasing decisions.

Future research should explore alternative enhancements to the as-cast structure, including alloying additions such as chromium, vanadium, or molybdenum, process modifications like centrifugal casting, or surface engineering techniques including laser melting or hard-facing, as these may improve wear resistance without destroying the beneficial chilled surface layer.

It is strongly recommended that future research include direct experimental validation of the theoretical wear estimates presented in this study, as the calculations are theoretical and have not been verified experimentally. Specifically, the following are recommended:

1. Direct ASTM G65-16 dry sand/rubber wheel abrasion testing on specimens from all experimental conditions to experimentally measure mass loss values and validate the theoretical calculations. The ASTM G65-16 standard should be followed without modification to ensure comparability with published data and standardised wear rankings.
2. Field trials to measure actual service life under real operating conditions.
3. SEM analysis of wear surfaces to confirm the inferred wear mechanisms.
4. Quantitative image analysis per ASTM E562-19 to verify phase fractions, particularly for microstructures that were inferred rather than directly observed in this study.
5. Migration testing per EN 1186-1:2002 to quantify metallic particle release and validate food safety implications.
6. Direct friction measurement through pin-on-disc or reciprocating tribometer testing to confirm the relationship between microstructure and friction behaviour.

To translate these research outcomes into practical improvements, collaborative efforts between manufacturers and researchers are encouraged, aimed at implementing enhanced production practices that will improve product quality, lower operational costs, and maintain food safety standards throughout West Africa.

Acknowledgements
The authors thank the Department of Metallurgical Engineering, The Federal Polytechnic, Offa, Nigeria, and the Federal University of Technology, Akure, Ondo State, Nigeria, for laboratory facilities and technical support, and the local manufacturer for supplying the grinding wheel samples.

References
1. Adebayo, A. O., Taiwo, G. L., & Oyetunji, A. (2017). Effects of magnesium variation and heat treatment on mechanical and micro-structural properties of ductile cast iron. FUOYE Journal of Engineering and Technology, *2*(2).
2. Adeyemi, O. O., & Ogunniyi, O. O. (2019). Casting defects and their influence on the service performance of locally manufactured grinding plates. West African Journal of Foundry and Metallurgy, *4*(1), 45-58.
3. Adeyemo, T., Onyekachi, A., & Chukwudi, E. (2023). Cooling rate effects on the microstructure of cast iron components. West African Journal of Materials Science, *9*(2), 134-151.
4. ASTM E10-18. (2018). Standard test method for Brinell hardness of metallic materials. ASTM International, West Conshohocken, PA.
5. ASTM E140-12b. (2012). Standard hardness conversion tables for metals relationship among Brinell hardness, Vickers hardness, Rockwell hardness, Superficial hardness, Knoop hardness, Scleroscope hardness, and Leeb hardness. ASTM International, West Conshohocken, PA.
6. ASTM E562-19. (2019). Standard test method for determining volume fraction by systematic manual point count. ASTM International, West Conshohocken, PA.
7. ASTM G65-16. (2016). Standard test method for measuring abrasion using the dry sand/rubber wheel apparatus. ASTM International, West Conshohocken, PA.
8. Busari, Y. O., Adebisi, J. A., Shuaib-Babata, Y. L., Amuzat, L. O., & Babamale, H. F. (2021). Effect of ferrochrome addition on wear and hardness properties of grey cast iron. Mindanao Journal of Science and Technology, *19*(2), 45-58.
9. Darmawan, A. S., Yulianto, A., Febriantoko, B. W., Masyrukan, Ginta, T. L., & Hamid, A. (2025). Engineering hardness and toughness of gray cast iron with the addition of silicon elements. Journal of Physics: Conference Series, *2972*(1), 012042. https://doi.org/10.1088/1742-6596/2972/1/012042
10. Doğan, O. N., & Hawk, J. A. (2001). Abrasion resistance of high chromium white irons. Journal of Materials Science, *36*(10), 2463-2473. https://doi.org/10.1023/A:1017963703610
11. EN 1186-1:2002. (2002). Materials and articles in contact with foodstuffs - Plastics - Part 1: Guide to the selection of conditions and test methods for overall migration. European Committee for Standardization, Brussels.
12. EN 12513:2011. (2011). Founding - Abrasion-resistant cast irons. European Committee for Standardization, Brussels.
13. Kaboli, K., Mostafapour, M., Kheirkhahan, N., Edalati, E., Solbi, E., Babakhani, A., & Kiani-Rashid, A. R. (2025). Revisiting the effect of casting thickness and austempering temperature of gray iron. Journal of Materials Engineering and Performance, *34*(14), 14167-14179. https://doi.org/10.1007/s11665-024-09999-9
14. Kibble, K. A., & Pearce, J. T. (2023). The effect of heat treatments on the properties of a ferritic high-chromium cast iron. Journal of Materials Engineering and Performance, *32*, 8262-8273. https://doi.org/10.1007/s11665-023-08099-4
15. Kostyleva, L. V., Gapich, D. S., Novikov, A. E., & Motorin, V. A. (2019). Variation of the composition and properties of cementite in heat treatment of tilling machine members from chilled cast iron. Metal Science and Heat Treatment, *61*(3-4), 205-210. https://doi.org/10.1007/s11041-019-00401-6
16. Kutelu, B. J., Oluyori, R. T., & Omoyeni, D. O. (2024). Microstructure characteristics and mechanical properties of grey cast iron at varied ferrosilicon addition. ABUAD Journal of Engineering Research and Development, *7*(2), 290-296.
17. Kwofie, S., & Chandler, H. D. (2016). Potential health effects of locally-manufactured corn-mill grinding plates. Journal of Science and Technology, *26*(2), 45-58.
18. Laird, G., Gundlach, R., & Röhrig, K. (2000). Abrasion-resistant cast iron handbook. American Foundry Society, Des Plaines, IL.

19. MEDID. (2025). Metal grinding discs for cast iron and steel [Product specifications]. MEDID Sp. z o.o. https://medid.pl/en/22-metal-grinding-discs
20. Ochulor, E. F., Adeosun, S. O., Kareem, A. J., & Ashade, A. I. (2023). Effects of annealing soaking time on carbide precipitates and mechanical properties of as-cast thin wall ductile iron. ABUAD Journal of Engineering Research and Development, *6*(2), 230-238.
21. Oke, S. R., & Ige, O. O. (2018). Assessment of locally fabricated grinding plates in Nigeria. Nigerian Journal of Technology, *37*(3), 678-685.
22. Omotoyinbo, J. A., & Oluwole, O. O. (2022). Corrosion behaviour of grinding discs in simulated gastro-intestinal environments. Journal of Materials and Corrosion, *73*(4), 567-578.
23. Oyewole, O. A., & Adebayo, A. A. (2020). Metallic contaminants in traditionally processed foods in Southwest Nigeria. Journal of Food Safety and Hygiene, *6*(3), 89-101.
24. Tabrett, C. P., Sare, I. R., & Ghomashchi, M. R. (1996). Microstructure-property relationships in high chromium white iron alloys. International Materials Reviews, *41*(2), 59-82. https://doi.org/10.1179/095066096790151195
25. Taiwo, F., Oyediran, O., & Akinwale, O. (2024). Influence of cooling rates on cast iron structure. Journal of Foundry and Casting Technology, *27*(3), 145-162.
26. Terngu, A., Agboola, O. F., & Garba, D. K. (2023). Model for prediction of some mechanical properties of ductile cast iron austempered in Jatropha curcas seed oil. Arid Zone Journal of Engineering, Technology and Environment, *19*(2), 203-210.
27. U.S. Food and Drug Administration. (2017). Food Code 2017: Chapter 4 - Equipment, utensils, and linens. U.S. Department of Health and Human Services, Washington, DC.
28. Widder, L., Rojacz, H., Buscher, M., & Varga, M. (2021). High-temperature abrasion resistance and wear mechanisms of chilled high-chromium cast irons. IOP Conference Series: Materials Science and Engineering, *1140*(1), 012027. https://doi.org/10.1088/1757-899X/1140/1/012027
29. Wilk, O. S., & Halle, T. (2023). Gruson's chilled cast iron - A legendary wonder material of the 19th century. Practical Metallurgy, *60*(12), 796-819. https://doi.org/10.1515/pm-2023-1046